HHS Public Access

Author manuscript

Nat Methods. Author manuscript; available in PMC 2019 March 10.

Published in final edited form as:

Nat Methods. 2018 October ; 15(10): 789–792. doi:10.1038/s41592-018-0115-y.

Three-Photon Imaging of Mouse Brain Structure and Function through the Intact Skull

Tianyu Wang[1,*], **Dimitre G. Ouzounov**[1], **Chunyan Wu**[1], **Nicholas G. Horton**[1], **Bin Zhang**[2], **Cheng-Hsun Wu**[2], **Yanping Zhang**[2,3], **Mark J. Schnitzer**[2,3], and **Chris Xu**[1,*]

[1]School of Applied and Engineering Physics, Cornell University, Ithaca, New York, USA

[2]*CNC* Program, Stanford University, Stanford, California, USA

[3]Howard Hughes Medical Institute, Stanford University, Stanford, California, USA

Optical imaging through the intact mouse skull is challenging because of the skull-induced aberration and scattering. We find that three-photon-excitation improves optical sectioning compared to two-photon-excitation, even with the same excitation wavelength and imaging system. Through the adult mouse skull, we demonstrate three-photon imaging of vasculature at >500μm depth, and GCaMP6-calcium imaging over weeks in cortical layers 2/3 and 4 in awake mice, with 8.5 frames/s and hundreds of micrometers field-of-view.

Observing the mouse brain in its native environment is critical to the study of neural network function and disease progression. Cranial window implantation and skull thinning[,] are the common minimally invasive procedures to obtain optical access to the mouse brain; however, they can still cause perturbation to the physiological environment in some cases. For example, mechanical stress during the surgeries induce unexpected activation of microglia and astrocytes[,]; skull openings change intracranial pressure and affects fluid flow in paravascular space, which may be important for waste disposal. Therefore, impoving imaging performance through the intact skull will open new opportunities to non-invasive brain research.

Non-fluorescence based technologies such as magnetic resonance imaging, photoacoustic tomography, and optical microaniography can map brain structure and hemodynamics below an intact skull. However, these technologies typically cannot achieve single-cell or sub-cellular resolution, and none of them is established for direct cellular activity measurement with high temporal resolution (e.g., > 1 Hz).

[*]Corresponding authors: tw329@cornell.edu and cx10@cornell.edu.

Author Contributions

C.X. conceived the study and supervised the project. T.W., D.G.O., and N.G.H. designed and performed the experiments. C.W. set up awake imaging and performed immunohistology. C-H. W., B.Z., and Y.Z. tested skull preparations for improving the optical transparency of the cranium for long-term imaging. C.X. and M.J.S. supervised the study. T.W. analyzed the data. T.W. and C.X. prepared the manuscript.

Competing Financial Interests

The authors declare no competing financial interests.

Data availability

The data that support the findings of this study are available from the corresponding author upon request

One-photon fluorescence can be used for imaging vasculature and neuronal activity through skull, either with infrared dyes, or skull clearing techniques[9]. However, such methods generally do not offer single-cell resolution, due to out-of-focus fluorescence excitation.

Two-photon microscopy (2PM) is routinely used for *in vivo* deep brain imaging for its optical sectioning capability in scattering media; however, 2PM has poor resolution when imaging through an intact skull. Although wavefront correction enabled 2PM to achieve submicron resolution, the corrected field-of-view (FOV) was about 23×23 μm and the imaging depth was limited to approximately 50 μm in the cortex. Recently, chemical treatment of the skull surface has been applied to improve the contrast of structural 2PM in the shallow cortex[9].

Three-photon microscopy (3PM) increases the imaging depth in the mouse brain because of the weaker scattering at longer excitation wavelengths and the background suppression by higher order nonlinear excitation, and 3PM imaging studies have revealed structure and function in the mouse hippocampus through cranial windows in intact brains[9]. Recently, vasculature imaging through the intact mouse skull was demonstrated with a synthesized dye of unusually large three-photon excitation (3PE) cross section at 1550 nm, reaching a depth of 300 μm. In this study, we show that 3PM not only achieves more than 500 μm cortical depth with conventional dyes but also is capable of calcium activity imaging at high spatial and temporal resolution with hundreds of micrometers FOV.

The refractive index of the cranial bone (~1.55) is significantly higher than that of water (1.32) or cerebrospinal fluid (~ 1.34). The high refractive index and the rough skull surface, especially after exposed to air, renders the skull opaque by scattering light like optical diffusers. We found that the skull surface roughness can be reduced by using an index-matching glue, which also seals the skull from the air and preserves transparency for chronic imaging (Fig. 1a, Supplementary Fig. 1). After the treatment, the effective attenuation length (l_e) of the skull was measured using the third harmonic generation (THG) signal from the osteocytes, and we found $l_e \sim 60$ μm at 1320 nm (Fig. 1).

We compared 2PM at 920 nm and 3PM at 1320 nm by imaging fluorescein-labeled vasculature of the same mouse, through the intact skull around the center of the parietal bone. 1320-nm 3PM resolved capillary vessels with high contrast (Fig. 1b), with signal-to-background ratio (SBR) close to 100 at 120 μm cortical depth, and ~ 10 at 510 μm (Fig. 1c). In comparison, 920-nm 2PM has substantially lower contrast, with tens of times higher background in the unlabeled region of the brain even at shallow depths (Fig. 1c). We verified that 920 nm generates negligible intrinsic autofluorescence in the emission band of fluorescein by imaging the mouse before any dye injection. Therefore, the background in 2PM is fluorescence from fluorescein.

To delineate the effects of longer wavelength and the higher order nonlinear excitation in through-skull imaging, we injected Alexa 680 into the same mouse, and immediately performed imaging by two-photon excitation (2PE) of Alexa 680 with 1320 nm, using the same laser and microscope. Figs. 1c and 1d indicate that the 1320-nm 2PM has similar SBR as 920-nm 2PM at all depths, with only limited improvement on contrast, presumably by the

reduced scattering and aberration at the longer excitation wavelength (Fig. 1b, the background was also verified to be fluorescence from Alexa 680). These results show that longer excitation wavelength alone is not sufficient, and 3PE is necessary for through-skull imaging.

With cranial windows, the SBR of 2PM remains high until the imaging depth is beyond approximately 4 scattering lengths. However, in our through-skull experiment, the SBR of 2PM, even with 1320 nm excitation, is below 10 immediately beneath the skull (Figs. 1c and 1d). The skull accounts for approximately 2 attenuation lengths, and has low labeling density due to the sparsity of vasculature in the bone. Therefore, the background in 2PM must be caused by the degradation of the point spread function (PSF), in both lateral (XY) and axial (Z) dimensions. For example, the lateral broadening of PSF is indicated by the blurred edges of capillaries in 2PM images (Fig. 1b); the axial elongation is indicated by the observation that large, penetrating blood vessels are much brighter relative to horizontal capillaries in 2PM than in 3PM (Fig. 1b). The higher order nonlinear excitation of 3PM is more effective in accentuating the central peak (i.e., the signal) and suppressing the unwanted fluorescence excitation from the side lobes (i.e., the background) of the PSF. Therefore, 3PE helps to preserve spatial resolution and improve image contrast with a degraded PSF. This explanation is further corroborated by the measured attenuation length of the brain tissue for through-skull imaging, which is shorter in 3PM than in 2PM (Fig. 1e, more discussion on the attenuation length is presented in the Supplementary Note 1).

To provide an upper bound estimate of the spatial resolution of through-skull imaging, we measured the fluorescence intensity profile of a dendrite (Figs 2a-d). The lateral and axial FWHM is 0.96 μm and 4.6 μm, respectively, which provides the upper bound of the spatial resolution due to the finite size of the neural processes. 2PM at 920 nm could not resolve any feature at high spatial resolution using the same GCaMP6 mice (Supplementary Fig. 2b).

We imaged spontaneous activities of GCaMP6s-labeled neurons in adult transgenic mice (*CamKII-tTA/tetO-GCaMP6s*, 8–12 weeks, including both male and female, N=5). Fig. 2e shows an imaging site in cortical layer 2/3 of an 8-week-old mouse with ~120-μm-thick skull. The neuronal activity traces were recorded under awake condition (Fig. 2f). The absolute signal-to-noise ratio (SNR) of the recording can be ascertained by the raw photon counts (Supplementary Fig. 3), which is comparable to typical 2PM calcium imaging through a cranial window. As imaging depth increases, the ΔF/F for through-skull 3PM appears to decrease due to increased background contribution (Fig. 1e). To maintain the SNR and temporal resolution, the photon counts per neuron per second must be increased by either delivering additional power to the focus or reducing the FOV. The deepest activity imaging in this study was at 465 μm below the cortical surface (Supplementary Fig. 4). While through-skull 3PM provides sufficient SNR for recording the activities with GCaMP6s in cortical layer 2/3 neurons, it requires much higher average and peak power than 2PM with cranial windows due to the combined effects of skull attenuation and the inefficient higher order nonlinear excitation. These power requirements ultimately limit the performance of through-skull 3PM (for a detailed discussion on the limits of 3PM through-skull imaging, see Supplementary Note 2). Therefore, 2PM imaging through cranial

windows remains the preferred method if the experimental results are not expected to be affected by the craniotomy.

We performed longitudinal study and recorded from the same neurons on 8 different days over a period of 4 weeks after the initial skull preparation (Supplementary Figs. 4a and 5 show longitudinal recordings from 3 sites at different depths). THG signal from the blood vessels was used to locate approximately the same imaging FOV for each recording session. Despite the long exposure time (cumulatively over 6 hours per recording site), no visible adverse effects had been observed on neuronal structure or activities, indicating the average power and the peak intensity were safe for imaging. We also performed immunostaining in the brains after imaging (Methods). The results confirmed that there is no measurable tissue damage under the imaging conditions for activity recording in this study (Supplementary Fig. 6). We observed some degradation of skull transparency over time, as indicated by the power needed to image the same sites (e.g. 35–50% more power after 4 weeks, Supplementary Fig. 5). Nonetheless, successful recordings of neuronal activity were performed for all imaging sessions.

In addition to 1320-nm 3PM, we tested 1700-nm 3PM for through-skull structural imaging using Texas Red labeled vasculature and red-fluorescent-protein labeled neurons, both reaching more than 500 μm cortical depth (Fig. 2g, Supplementary Fig. 7).

We have demonstrated through-skull 3PM of mouse brain structure and function, with high spatial and temporal resolution, large FOV, and at significant depth. Furthermore, by comparing 2PM and 3PM at the same excitation wavelength, we show unequivocally that 3PE is necessary for imaging through the intact skull, regardless of the imaging depth and the labeling density. This work demonstrates the advantage of higher order nonlinear excitation for imaging through a highly scattering layer, which is in addition to the previously reported advantage of 3PM in deep imaging of densely labeled samples. The demonstrated technique will open new opportunities for non-invasive studies of living biological systems.

Online Method Section

Experimental set up:

The laser and microscope setup is similar to that in our previous work. Any difference in system parameters is stated in this method section.

Excitation source: The excitation source for 1320-nm 3PM is a noncollinear optical parametric amplifier (NOPA, Spectra Physics) pumped by a regenerative amplifier (Spirit, Spectra Physics). A two-prism (SF11 glass) compressor is used to compensate for the normal dispersion of the optics of the light source and the microscope, including the objective. The NOPA operates at wavelength centered at 1320 nm, and provides an average power of ~ 700 mW (1750 nJ per pulse at 400 kHz repetition rate). The pulse duration (measured by second-order interferometric autocorrelation) under the objective is ~ 37 fs after optimizing the prism compressor. An optical delayed line is used to double the laser

repetition rate to 800 kHz, by splitting the excitation beam into two of equal powers and introducing ~ 10 ns delay between their pulse trains.

The excitation source for 2PM is a mode-locked Ti:Sapphire laser (Tsunami, Spectra Physics) centered at 920 nm. The 920-nm beam and 1300-nm beam are spatially overlapped and directed to the same microscope, and then combined by a dichroic mirror.

The excitation source for 1700-nm 3PM was solitons centered at 1700 nm generated by soliton self-frequency shift in a photonic crystal fiber pumped by a fiber laser at 1550nm. The excitation source was described in more detail in ref. .

Imaging setup: The images were taken with a custom-built multiphoton microscope with a high-numerical aperture objective (Olympus XLPLN25XWMP2, 25X, NA 1.05). The objective was under-filled to reduce unnecessary loss of power in the marginal rays, and the $1/e^2$ beam diameter of the excitation beam was ~11 mm, which is ~70% of the objective back aperture diameter.

The signal is epi-collected through the objective and then reflected by a dichroic beam splitter (FF705-Di01–25×36, Semrock) to the detection system. There are two detection channels: one for fluorescence signal and the other for third harmonic generation (THG). For GCaMP6s imaging, we used a photomultiplier tube (PMT) with GaAsP photocathode (H7422–40, Hamamatsu) for the fluorescent signal and an ultra bialkali PMT (R7600–200, Hamamatsu) for the THG signal. A 488-nm dichroic beam splitter (Di02-R488–25×36, Semrock) was inserted at 45 degrees to the signal beam path to separate and direct fluorescence and THG to their respective PMTs. Fluorescence generated by fluorescein and GCaMP6s was selected by a 520±30 nm band-pass filter (Semrock), and THG around 440 nm was selected by a 435±20 nm filter (Semrock). For Alexa 680 imaging, we switched to a GaAs PMT (H7422–50, Hamamatsu) for the fluorescence channel, which has higher sensitivity at longer wavelength. The fluorescence filter was also changed to 716±20 nm (Semrock) filter to pass Alexa 680 fluorescence while blocking the second harmonic of 1320 nm.

For signal sampling, the PMT current is converted to voltage by a transimpedance amplifier with 10MHz bandwidth (C9999, Hamamatsu), providing adequate temporal resolution for photon counting. For analog signal acquisition, an additional 1.9 MHz low pass filter (Minicircuts, BLP-1.9+) is used before digital sampling. Analog-to-digital conversion is performed by a data acquisition card (NI PCI-6115, National Instruments). The signal acquisition system displayed shot-noise limited performance, and light shielding was carefully done to achieve dark counts of 20–40 photons per second under actual imaging conditions without laser scanning. ScanImage 3.8 running on MATLAB (MathWorks) was used to acquire images and control a 3D translation stage to move the sample (M-285, Sutter Instrument Company). All imaging depths and thickness are reported in raw axial movement of the motorized stage, unless otherwise stated. The refractive indices of skull and brain tissue (1.55 for the bone and 1.35 to 1.37 for the cortex) are higher than that of water (1.32), which result in slight under-estimate of the actual depth in the experiments (~ 12% for the skull thickness and ~3% for the depth in the brain tissue).

High resolution structural images were typically taken with 512×512 pixels/frame, 0.5 Hz frame rate, and multiple frame averages at each depth. Neuronal activities were recorded using 256×256 pixels/frame at 8.49 Hz frame rate. Each site was recorded for 30 to 50 minutes in each imaging session. The conversion from pixel values to photon counts was performed according to the method described in the previous publication.

For in vivo imaging, the mouse was placed on a tip-tilt stage under the objective lens, and it is important to ensure the skull surface and the coverslip is parallel to the imaging plane of the objective. In most cases, the skull is curved, and it is preferable to adjust the tilt angle so that the apex of the curvature is directly above the imaging site.

Resolution Measurement on Dendrites: To eliminate the fluctuation in brightness caused by changing calcium concentration, a neuron was intentionally damaged by continuous laser scanning for 4 minutes at high intensity (~9 nJ at the focus) and small FOV (20 μm x 20 μm). The damaged neuron has a constant brightness for the GCaMP6s fluorescence. A z-stack was then taken around the soma and its apical dendrites at 0.2 μm step. Intensity profiles of the dendrite were plotted either laterally or axially to estimate the resolution.

Image Processing for Activity Recording: Mechanical drift in the horizontal plane, if any, was corrected by TurboReg plug-in in ImageJ. Regions of interest (ROIs) were generated by manual segmentation of neuron bodies. In MATLAB, fluorescence intensity traces were low-pass filtered with a hamming window of a time constant of 1.06 s. Spikes were inferred according to ref. 24 assuming shot-noise limited detection. Baselines of the traces (F_0) were then determined by excluding the spikes as well as their rising and falling edges. Traces (F) were normalized according to the formula $(F- F_0)/F_0$. Examples of the raw activity recording videos played at the recording frame rate of 8.49 Hz with 2 frames rolling average are presented in Supplementary Video 1. For visual representation of calcium activities in Supplementary Video 2, raw image sequence was first rolling averaged with 17 frames, and then the local background was subtracted to improve contrast (ImageJ). The activity movie was further processed by Kalman filter with a gain from 0.7–0.9 for noise reduction (ImageJ).

Image Processing for Structural Imaging: Structural images were processed with a median filter of 1-pixel radius, and then normalized by linear transform of pixel intensities to saturate the brightest 0.2–0.5% pixels of each frame. Three-dimensional reconstruction of the stacks was rendered in Volocity (version 6.3). For the purpose of visualization, some of the high-resolution images in Fig. 2e, Supplementary Fig. 4 and 5 were displayed with a gamma correction value of 0.8–0.95 to reduce brightness contrast between different neurons.

Statistics and Data Analysis: All data analysis was performed in MATLAB 2016. The effective attenuation length in Fig. 1e was derived by least-square linear regression of fluorescent signal data. For all representative results, the number of successful independent experiments on different animals is indicated in the corresponding figure legend, and more details on the ages of the animals are included in “Life Sciences Reporting Summary”.

Animal Procedures

All animal experimentation and housing procedures were conducted in accordance with Cornell

University Institutional Animal Care and Use Committee guidance.

Skull Preparation for Chronic Imaging: Before the surgery, animals were anesthetized with isoflurane (3% in oxygen for induction, and 1.5–2% for surgery to maintain a breathing frequency around 1 Hz). Body temperature was kept at 37.5 °C with a feed-back controlled blanket (Harvard Apparatus), and eyes were covered with eye ointment. Glycopyrrolate (0.01mg/kg body weight), dexamethasone (0.2mg/kg body weight), and ketoprofen (5mg/kg body weight) were administrated intramuscularly. Dexamethasone and ketoprofen were also administrated in two consecutive days following the surgery. The anesthetized animal was fixed on stereotaxic, and hair was removed from scalp with scissors and Nair. The scalp was further sterilized by alcohol wipes, and then cut open and removed to expose both parietal plates as well as the bregma and lambda. Sterile saline was applied to the skull immediately after the exposure, and it is critical to keep the entire bone surface covered by saline to insulate from air. Fascia and connective tissue on the skull were gently removed with forceps and sterile wet cotton tips to avoid any internal bleeding inside the brain. At this point, the whole skull was transparent, with blood vessels underneath visible with sharp edges. The saline covering the skull was then wiped completely dry with cotton tips, and the following actions were taken quickly before the bone turns opaque. Ultra-violet curable glue (Loctite 4305) was applied to the skull surface within 2 seconds afterwards. A sterile and dry round coverslip of 5-mm diameter (#1 thickness, Electron Microscopy Sciences) was placed on the skull, centered at 2.5 mm lateral, and 2 mm caudal from the bregma point. The coverslip was pressed closely against the skull surface by forceps to minimize the amount of glue between the coverslip and the skull. The glue was left to cure by itself for about 5 minutes without any ultra-violet light, during which time the skull transparency tends to increase visually. Afterwards, an ultra-violet light source (385–515nm, Bluephase Style 20i, Ivoclar vivadent) was used to completely cure the glue, with roughly 1s on and 1s off for 3s. The coverslip is necessary to keep the glue layer as thin as possible (down to ~10 μm at the thinnest part on the skull), and to form a flat interface to reduce aberration. The exposed part of the skull surrounding the coverslip was further covered with dental cement. Supplementary Fig. 1 shows an example of successful preparation. For awake imaging, a head-bar for head fixation during imaging was glued to the exposed parts of the skull surrounding the coverslip by metabond glue.

Imaging Procedures: For imaging of anesthetized animal, the mice were anesthetized using isoflurane (1–1.5 % in oxygen, maintaining a breathing frequency at 2 Hz) and placed on a heat blanket to maintain body temperature at 37.5 °C. Eye ointment was applied and the animal was place on a 3D motorized stage for navigation under the microscope. For structural imaging, vasculature of wild-type mice (N=3, 10–12 weeks, male, C57BL/6J, The Jackson Laboratories) was labeled through retro-orbital injection with fluorescein, Alexa 680, and Texas Red (25mg dextran conjugate dissolved in 200 μl sterile saline, 10kDa molecular weight, Invitrogen).

For awake imaging, the animal was fixed on a custom-made stereotaxic plate by attaching its head-bar to the metal holders. The body of the animal was further secured in a tube of slippery inner walls to reduce motion.

Immunohistochemistry for tissue damage assessment: Anesthetized mice were continuously imaged with 1320-nm 3PM with the laser operating at 400 kHz repetition rate. The scanned region is located at ~2.5-mm lateral and 1-mm caudal to the bregma point. A 200×200 μm FOV at ~200-μm cortical depth was continuously scanned for 30 minutes, at 60 mW average power under the objective lens for one mouse and at 120 mW for the other. After 16 hours, mice were transcardially perfused, and the brains were postfixed. The brain fixation and antibody staining procedures followed the protocol as described in a previous work (detailed information on the antibodies used in this study is included in "Life Sciences Reporting Summary"). Coronal sections were cut in 50-μm thickness step through the center of the imaged region, and alternating slices were labeled for heat shock protein (HSP) and glial fibrillary acidic protein (GFAP). The brain slices were imaged with a Zeiss 780 confocal microscope.

Supplementary Material

Refer to Web version on PubMed Central for supplementary material.

Acknowledgments

We thank members of the Xu group and Schnitzer Lab for discussion. We thank Kaspar Podgorski and Amy Hu at Janelia Farm for advices on tissue damage assessment. We also thank Hong Goo Chae and Dinu Florin Albeanu at Cold Spring Harbor for sharing the head-bar and holder design for awake imaging. Last, we thank Warden lab at Cornell for providing microtome for brain sectioning.

The project was supported by DARPA W911NF-14–1-0012 to C. X., NIH/NINDS U01NS090530 to C. X., National Science Foundation NeuroNex Grant DBI-1707312 to C. X., and DARPA HR0011–16-2–0017 to M.J.S.

Supported by the Intelligence Advanced Research Projects Activity (IARPA) via Department of Interior/Interior Business Center (DoI/IBC) contract number D16PC00003 to C. X.. The U.S. Government is authorized to reproduce and distribute reprints for Governmental purposes notwithstanding any copyright annotation thereon. Disclaimer: The views and conclusions contained herein are those of the authors and should not be interpreted as necessarily representing the official policies or endorsements, either expressed or implied, of IARPA, DoI/IBC, or the U.S. Government.

References

1. McGonigle P Animal models of CNS disorders. Biochem. Pharmacol 87, 140–149 (2014). [PubMed: 23811310]
2. Holtmaat A et al. Long-term, high-resolution imaging in the mouse neocortex through a chronic cranial window. Nat. Protoc 4, 1128–1144 (2009). [PubMed: 19617885]
3. Yang G, Pan F, Parkhurst CN, Grutzendler J & Gan W-B Thinned-skull cranial window technique for long-term imaging of the cortex in live mice. Nat. Protoc 5, 201–208 (2010). [PubMed: 20134419]
4. Drew PJ et al. Chronic optical access through a polished and reinforced thinned skull. Nat. Methods 7, 981–984 (2010). [PubMed: 20966916]
5. Dorand RD, Barkauskas DS, Evans TA, Petrosiute A & Huang AY Comparison of intravital thinned skull and cranial window approaches to study CNS immunobiology in the mouse cortex. IntraVital 3, e29728 (2014). [PubMed: 25568834]

6. Thrane VR et al. Paravascular microcirculation facilitates rapid lipid transport and astrocyte signaling in the brain. Sci. Rep 3, 2582 (2013). [PubMed: 24002448]
7. Jonckers E, Shah D, Hamaide J, Verhoye M & Van der Linden A The power of using functional fMRI on small rodents to study brain pharmacology and disease. Front. Pharmacol. 6, 1–19 (2015). [PubMed: 25805991]
8. Wang X, Pang Y, Ku G, Stoica G & Wang LV Three-dimensional laser-induced photoacoustic tomography of mouse brain with the skin and skull intact. Opt. Lett 28, 1739–1741 (2003). [PubMed: 14514085]
9. Wang RK et al. Three dimensional optical angiography. Opt. Express 15, 4083 (2007). [PubMed: 19532651]
10. Hong G et al. Through-skull fluorescence imaging of the brain in a new near-infrared window. Nat. Photonics 8, 723–730 (2014). [PubMed: 27642366]
11. Silasi G, Xiao D, Vanni MP, Chen ACN & Murphy TH Intact skull chronic windows for mesoscopic wide-field imaging in awake mice. J. Neurosci. Methods 267, 141–149 (2016). [PubMed: 27102043]
12. Steinzeig A, Molotkov D & Castrén E Chronic imaging through 'transparent skull' in mice. PLoS One 12, e0181788 (2017). [PubMed: 28813435]
13. Theer P & Denk W On the fundamental imaging-depth limit in two-photon microscopy. J. Opt. Soc. Am. A 23, 3139–3149 (2006).
14. Park J-H, Sun W & Cui M High-resolution in vivo imaging of mouse brain through the intact skull. Proc. Natl. Acad. Sci 112, 9236–9241 (2015). [PubMed: 26170286]
15. Zhao Y-J et al. Skull optical clearing window for in vivo imaging of the mouse cortex at synaptic resolution. Light Sci. Appl 7, 17153 (2018).
16. Zhang C et al. A large, switchable optical clearing skull window for cerebrovascular imaging. Theranostics 8, 2696–2708 (2018). [PubMed: 29774069]
17. Horton NG et al. In vivo three-photon microscopy of subcortical structures within an intact mouse brain. 7, 205–209 (2013).
18. Ouzounov DG et al. In vivo three-photon imaging of activity of GCaMP6-labeled neurons deep in intact mouse brain. Nat. Methods 14, 388–390 (2017). [PubMed: 28218900]
19. Wang Y et al. Aggregation-Induced Emission Luminogen with Deep-Red Emission for Through-Skull Three-Photon Fluorescence Imaging of Mouse. ACS Nano acsnano.7b05645 (2017). doi: 10.1021/acsnano.7b05645
20. Ascenzi A & Fabry C Technique for Dissection and Measurement of Refractive Index of Osteones. J Biophys Biochem Cytol. 6, 139–142 (1959). [PubMed: 13673068]
21. Tuchin VV Methods and algorithms for the measurements of optical parameters of tissues. Tissue Opt. Light Scatt. Methods Instruments Med. Diagnosis 143–256 (2000).
22. Horton NG & Xu C Dispersion compensation in three-photon fluorescence microscopy at 1,700 nm. Biomed. Opt. Express 6, 1392 (2015). [PubMed: 25909022]
23. Yuryev M et al. In vivo Calcium Imaging of Evoked Calcium Waves in the Embryonic Cortex. Front. Cell. Neurosci 9, 1–9 (2016).
24. Podgorski K & Ranganathan G Brain heating induced by near infrared lasers during multi-photon microscopy. bioRxiv 057364 (2016). doi:10.1101/057364

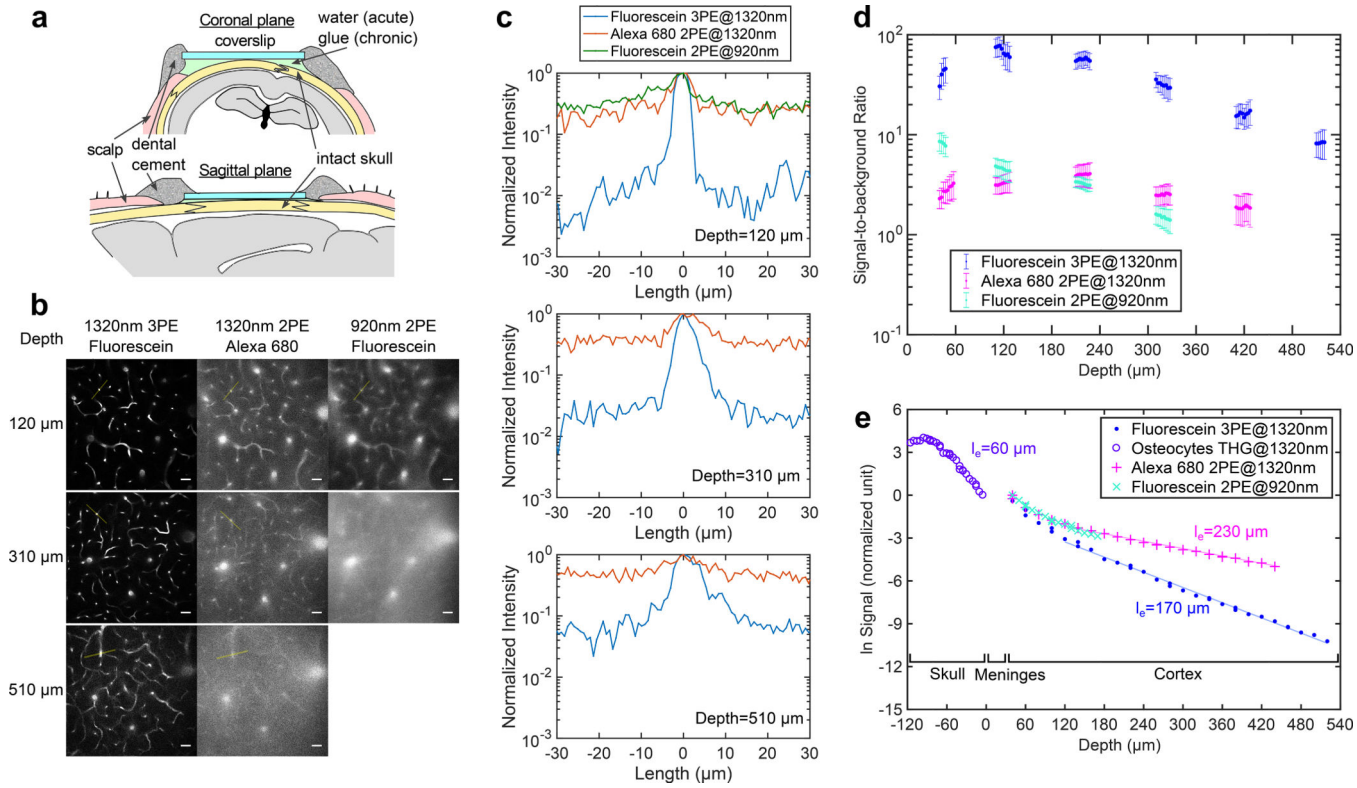

Figure 1|. Comparison of Through-skull Vasculature Imaging by 3PM and 2PM.

a, Schematic of through-skull imaging preparation with sagittal and coronal views (photos of a good preparation are shown in Supplementary Fig. 1).

b, Comparison of 2PM and 3PM images of vasculature of a wild-type mouse (C57BL/6J, male, 12 weeks, similar results n=3) in the same cortical column under the central area of a parietal bone, with chronic preparation. Each site was imaged by 920-nm 2PE of fluorescein, 1320-nm 3PE of fluorescein and 1320-nm 2PE of Alexa680 during the same imaging session. For 920-nm 2PM, 510 μm depth is not shown since the maximum imaging depth achieved was 420 μm (Supplementary Fig. 2). Each frame was integrated for 50 s to ensure photon shot noise is negligible, and all image contrasts were linearly stretched to saturate top 0.2% pixels. Scale bar, 30 μm.

c, Intensity profiles across the brightest blood vessels in each frame in (**b**), along the yellow lines (similar results n=3).

d, SBR measured at different depths for the three imaging groups in (**b**) (similar results n=2). The signal was calculated from the average of the top 0.1% brightest pixels in each frame, and background from the average of the unlabeled regions. Each data point was calculated from one image, and the vertical error bar indicates the standard deviation of SBR, originated from the brightness variation of blood vessels in each image.

e, Signal attenuation with depth for through-skull vasculature imaging measured in the same mouse as in (**b**) (similar results, n=2). Meninges include dura mater, arachnoid and pia mater. The signal strength at a particular depth is represented by the average value of the brightest 0.5% of the pixels in the x-y image from that depth. The effective attenuation

length l_e was determined by the exponential fit of the signal as a function of imaging depth (THG signal was used inside the skull). Each data point was calculated from one image.

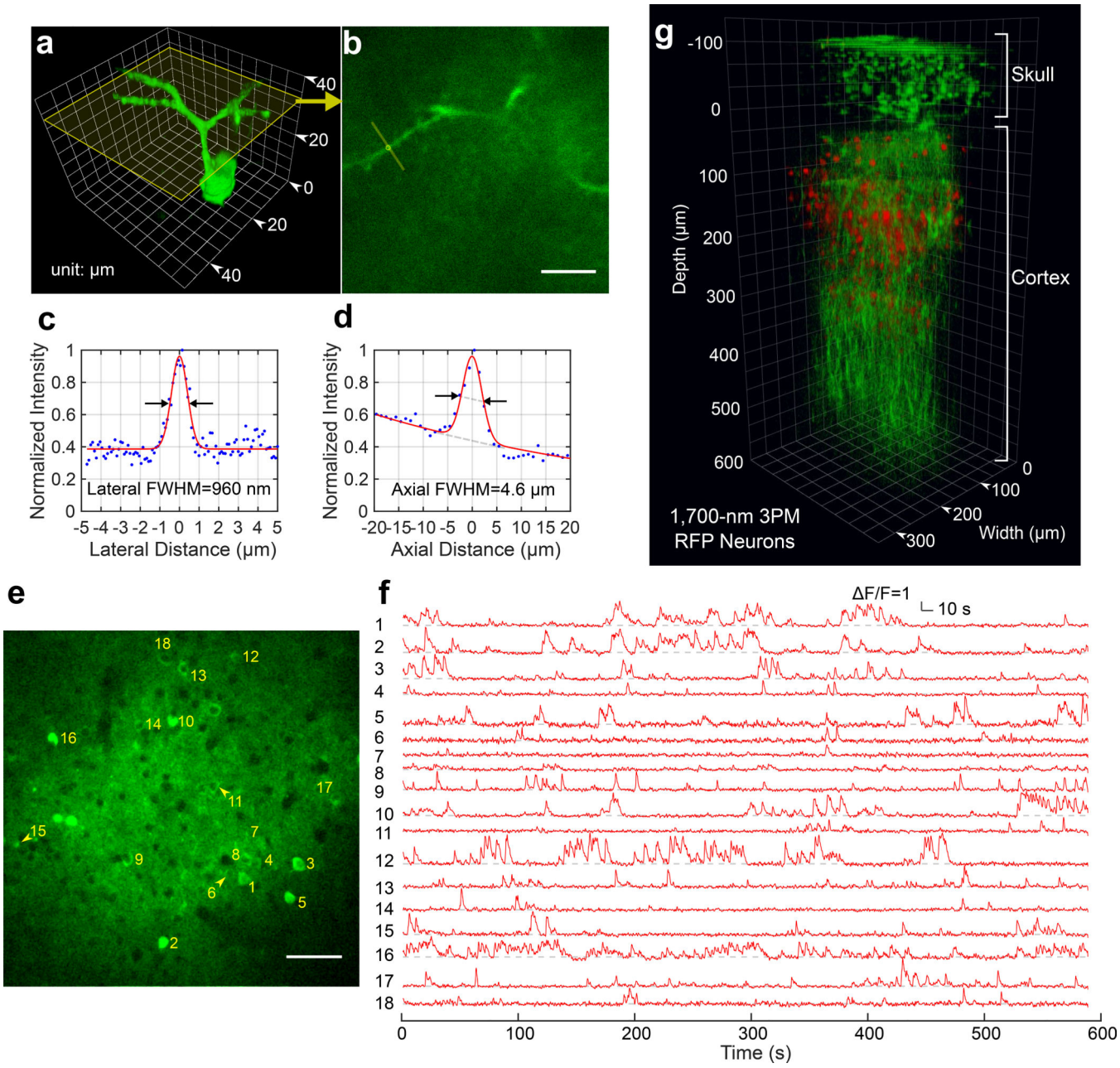

Figure 2|. Through-skull Imaging of Neural Structure and Function

a, 3D reconstruction of a GCaMP6s-labeled neuron located about 140 μm below the cortical surface of a transgenic mouse (*CamKII-tTA/tetO-GCaMP6s*, 10 weeks; similar measurements were performed on 2 mice with 3 neurons each, in total n=6) imaged by 1320-nm 3PM through the intact skull (thickenss ~ 100 μm). Apical dendrites can be clearly observed for resolution estimation.

b, A cross section of the 3D stack in (**a**), with its location indicated by the yellow frame in (**a**). The locations for lateral and axial resolution measurement on the apical dendrite are indicated by the yellow line and circle, respectively (similar results n=6). Scale bar, 10 μm.

c, Lateral intensity profile measured along the yellow line in (**b**), fitted by a Gaussian profile for the estimation of the lateral resolution (similar results n=6).
d, Axial intensity profile measured in the region within the yellow circle in (**b**), fitted by the sum of two Gaussian profiles, with one broad, off-centered Gaussian profile to corrected for the uneven baseline, and the other for the central peak (similar results n=6).
e, High resolution image of a site for through-skull activity recording in an awake, GCaMP6s-labeled transgenic mouse (*CamKII-tTA/tetO-GCaMP6s*, female, 8 weeks, similar results n=5). The recording site is about 275 μm below the cortical surface and the FOV was 320 μm × 320 μm (256×256 pixels per frame). Scale bar, 50 μm
f, Spontaneous activity traces recorded under awake condition from the indexed neurons in (**e**), acquired at 8.49 Hz frame rate (similar results n=5). The repetition rate used for imaging was 800 kHz, and the average power under the objective lens was 44 mW. Each trace is normalized to its baseline and low-pass filtered by a hamming window of 1.06 s time constant. The same site was visited 8 times over a period of 4 weeks after the skull preparation, with cumulatively over 6 hours of recording time (data from other imaging sessions are shown in Supplementary Fig. 5).
g, 3D reconstruction of through-skull imaging of a cortical column of red fluorescent protein (RFP) labeled neurons in a Brainbow mouse (*B6.Cg-Tg*(*Thy1-Brainbow1.0)HLich/J*, male, 12 weeks, similar results n=2). The red channel is 3PE fluorescent signal from RFP and the green channel is THG. The zero depth is set just beneath the skull.